The magnetotelluric tensor: improved invariants for its decomposition, especially 'the 7th'

Frederick E. M. Lilley

Research School of Earth Sciences, Australian National University, Canberra, ACT 0200, Australia.
Email: ted.lilley@anu.edu.au

Abstract.   A decomposition of the magnetotelluric tensor is described in terms of quantities which are invariant to the rotation of observing axes, and which also are distinct measures of the 1D, 2D or 3D characteristics of the tensor and so may be useful in dimensionality analysis. When the in-phase and quadrature parts of the tensor are analysed separately there are two invariants which gauge 1D structure, two invariants which gauge 2D structure, and three invariants which gauge 3D structure. A matrix method similar to singular value decomposition is used to determine many of the invariants, and their display is then possible on Mohr diagrams. A particular set of invariants proposed some seventeen years ago is revised to yield an improved set. Several possibilities for the seventh invariant are canvassed, and illustrated by examples from field data. Low values of $\Delta\beta$, the invariant now preferred for 'the 7th', may indicate a particular simplification of otherwise complicated three-dimensional structure.

Introduction

The magnetotelluric (MT) method of geophysics exploits the phenomenon of natural electromagnetic induction which takes place at and near the surface of Earth. The purpose is to determine information about the electrical conductivity structure of Earth, upon which the process of electromagnetic induction depends. The MT method has been well described recently in books by Simpson and Bahr (2005), Berdichevsky and Dmitriev (2008) and Chave and Jones (2012). The reader is referred to these publications for general information about the method and its results.

In the most simple form of the method, data are observed as time-series at a single field site. Typically three components (north, east and vertically downwards) of the fluctuating magnetic field are observed, and two components (north and east) of the fluctuating electric field. The electric field is measured between grounded electrodes typically several hundred metres apart. Strong static vertical electric fields may exist between clouds in the atmosphere and Earth's surface (Young and Freedman, 2016: 766) and occasionally be discharged by lightning strikes. Generally, however, the local fluctuating vertical electric field is taken as zero, because no current which is due to electromagnetic induction in the Earth flows vertically at the ground-air interface.

The traditional MT method expresses the two horizontal electric field components as linear functions of the two horizontal magnetic field components. The natural signals observed cover a frequency band from 0.001 to 1000 Hz. The signals have a variety of causes, the relative importance of which varies with position on the Earth, especially latitude. Recorded data are transformed to the frequency domain, and interpretation proceeds based on frequency dependence.

The reduction of observed time-series to the frequency domain is thus fundamental to the MT method. In the frequency domain various transfer functions are determined, encapsulating the response of the observing site to the source fields causing the induction.

Electromagnetic theory predicts that observed data will have particular qualities if the geological structure in which the induction is occurring has simplifying electrical-conductivity characteristics. For the most general case of no simplifying characteristics, below ground surface the geological electrical conductivity varies in all three possible space dimensions, and is denoted 3D. The simpler 'two dimensional' or 2D case arises when there is one particular horizontal direction in which the electrical conductivity does not vary; this direction of constant conductivity structure is then the 'strike' of the 2D structure.

The one dimensional or 1D case arises when the conductivity below ground level varies with depth only, and may be described as 'horizontally layered'. There is then no variation in any horizontal direction. The case of general uniform conductivity, i.e. no variation with depth either, is also commonly described as 1D.

A fundamental part of the data-reduction process arises as the 'rotation' of observed data. By 'rotation' is meant an examination of the observed transfer functions, to calculate the values they would take were the observing axes to be physically rotated. The purposes of rotation are to expose evidence of geologic dimensionality in the data; to give values of strike direction in the case of 2D data; and to give 'nearest strike direction' (in some sense) if the data, though 3D, may be approximated as 2D.

When taking and analysing the in-phase and out-of-phase ('quadrature') parts of a tensor separately, frequency by frequency, the Mohr diagram representation is an informative way to display the results, and to distinguish the different cases of 1D, 2D and 3D electrical conductivity structure. Various

quantities which do not vary when the axes are rotated, and so are 'rotational invariants', are obvious on a Mohr diagram.

The 2×2 structure of the MT tensor means it is also well-suited to analysis by the methods of linear algebra. A method which reduces a tensor to 2D form by anti-diagonalisation is very similar to traditional singular value decomposition (SVD), and is found to give one of the sets of invariants displayed on Mohr diagrams.

Three tensors are basic in contemporary MT practice. They are the distortion tensor as discussed by Lilley (2016); the MT tensor as discussed in this paper; and the 'phase tensor' of Caldwell et al. (2004), the invariants of which it is intended to review in a third and subsequent paper of this series.

Notation

Denoting by **E** and **H** respectively the electric and magnetic fluctuations at an observing site on the surface of Earth, the common representation of the magnetotelluric tensor **Z** which links these fluctuating fields is

$$\mathbf{E} = \mathbf{ZH} \tag{1}$$

of components

$$\begin{bmatrix} Ex \\ Ey \end{bmatrix} = \begin{bmatrix} Zxx & Zxy \\ Zyx & Zyy \end{bmatrix} \begin{bmatrix} Hx \\ Hy \end{bmatrix} \tag{2}$$

The original electric and magnetic fluctuation data are recorded as time-series, and then transformed to the frequency domain. In Equations 1 and 2 all quantities are complex functions of frequency ω, and a time dependence of $\exp(i\omega t)$ is understood.

In this paper the subscripts p and q will be used to denote in-phase and quadrature parts of a complex quantity. For example the complex quantity Zxy in Equation 2 is expressed

$$Zxy = Zxy_p + i\,Zxy_q \tag{3}$$

Note that adopting the (equally valid) time-dependence of $\exp(-i\omega t)$ would change the sign of Zxy_q. Such a change of sign may be misinterpreted if its cause is not clearly understood, especially in the context of strong distortion. Thus when using established computer procedures for the time-series analysis of observed data it is important to be clear on whether those procedures are based on a time dependence of $\exp(i\omega t)$ or $\exp(-i\omega t)$.

The subscripts p and q will also be used to denote quantities which are derived from the in-phase and quadrature parts respectively of complex quantities, but which are themselves not recombined to give a further complex quantity. Examples are the quantities C_p and C_q, to be introduced below.

Also in this paper, for compactness of text, a 2×2 matrix such as that for **Z** in Equation 2 will in places be written [Zxx, Zxy; Zyx, Zyy]. A rotation matrix $\boldsymbol{R}(\theta)$ will be introduced

$$\boldsymbol{R}(\theta) = [\cos\theta, \sin\theta; -\sin\theta, \cos\theta] \tag{4}$$

Units of **E**, **Z** and **H**

Following the International System (SI) (and see also Hobbs (1992)), the units of electric field **E** are *volt/metre* (V/m); of magnetic intensity **H** are *ampere/metre* (A/m); and of the elements of **Z** are *ohm* (Ω). When thus determined from **E** and **H** measured in the units described, **Z** is the 'magnetotelluric impedance tensor' (Weidelt and Chave, 2012: 124).

However, often the magnetic field is observed with apparatus which gives a measurement of the magnetic induction **B** in units of *tesla*. Using such magnetic induction values rather

than magnetic intensity values to determine **Z** then gives the 'magnetotelluric response tensor' (Weidelt and Chave, 2012).

Further there is a tradition of observation in 'practical field units', for which the electric field is measured in *millivolt/kilometre* (mV/km), and the magnetic induction is measured in *nanotesla*.

Under these circumstances, invoking the relationship

$$\mathbf{B} = \mu_o\mathbf{H} \tag{5}$$

(where μ_o is the permeability of free space and has the value $4\pi \times 10^{-7}$ in the SI units of *henry/metre*) allows response tensor values to be converted to impedance tensor values. The following conversion factors may be useful.

Firstly let Z_1 be the numerical value of a tensor element determined by values of **E** measured in V/m and of **H** measured in A/m. Secondly let Z_2 be the numerical value of the same impedance element determined by values of **E** measured in V/m and of **B** measured in *tesla*. Thirdly let Z_3 be the numerical value of the same impedance element determined by values of **E** measured in mV/km and of **B** measured in *nanotesla*. Then:

$$Z_1 = Z_2 \times 4\pi \times 10^{-7} \tag{6}$$

and

$$Z_1 = Z_3 \times 4\pi \times 10^{-4} \tag{7}$$

The components of **Z** (such as Zxy) are often converted to and quoted as values of 'apparent resistivity', in units of Ωm. This practice arises from the case of the simple structure of a uniform half-space. Theory shows that the (true) resistivity ρ in Ωm of such a half-space is given by

$$\rho = \frac{1}{\omega\mu}\left|\frac{E}{H}\right|^2 \tag{8}$$

where the electric and magnetic fields E (in V/m) and H (in A/m), fluctuating at angular frequency ω, are measured on the half-space surface at right angles to each other, and where the permeability μ may be taken as that for free space (μ_o) as above.

When the resistivity structure is more complicated, the presentation of observed data as apparent resistivity ρ_a, again in Ωm, is often still found to be useful. Thus, for example, an apparent resistivity ρ_{aZxy} for the Zxy component of the tensor may be expressed as

$$\rho_{aZxy} = \frac{1}{\omega\mu}|Zxy|^2 \tag{9}$$

and calculated as

$$\rho_{aZxy} = \frac{1}{\omega\mu}\left(Zxy_p{}^2 + Zxy_q{}^2\right) \tag{10}$$

A phase ϕ_{Zxy} for ρ_{aZxy} may be calculated as

$$\phi_{Zxy} = \arctan\left(\frac{Zxy_q}{Zxy_p}\right) \tag{11}$$

where the signs of Zxy_p and Zxy_q may be taken into account to give a phase value over a range of $360°$.

When the tensor element Zxy is evaluated in the practical units of mV/km/nanotesla, Equation 9 takes the well-known form

$$\rho_{aZxy} = 0.2\,T|Zxy|^2 \tag{12}$$

again giving the apparent resistivity in Ωm, where T is the period in seconds (s), i.e. $T = 2\pi/\omega$. Equations 9 and 12 show

that for the case of uniform resistivity, Zxy will have a period dependence of $T^{-1/2}$. Such a $T^{-1/2}$ dependence of Zxy is often approximately the case generally, and to take it into account there may be a benefit in presenting the quantity $Zxy\,T^{1/2}$ rather than the quantity Zxy, as will be shown in some examples below. At high frequencies at many sites MT observations sense the surface layer as a 1D structure, and in such cases the calculated apparent resistivity of this layer may be a helpful benchmark in interpretation.

Finally it should be emphasised that the units taken for $\mathbf{Z}$ in Equation 1 can be chosen to be those which are most useful. The important matter when interpreting MT data, for instance by fitting models, is that the responses of such models are calculated in the same units as those of the observed data. To expand this point further, when interpreting MT data there may be occasions when modelling rotational invariants, rather than modelling the (rotation-dependent) observed tensor elements, may be constructive.

It may also be pertinent to note that when tensor elements are calculated in the units of Ω, Equation 8 above cautions strongly against any temptation to regard such numbers as a 'rule of thumb' estimate of the apparent resistivity of the material in Ωm.

The MT tensor upon rotation of the horizontal axes

Upon rotation of the horizontal measuring axes clockwise by angle θ' as shown in Figure 1, Equation 1 changes to

$$\mathbf{E}' = \mathbf{Z}'\mathbf{H}' \tag{13}$$

where

$$\mathbf{E}' = \mathbf{R}(\boldsymbol{\theta}')\mathbf{E} \tag{14}$$

$$\mathbf{H}' = \mathbf{R}(\boldsymbol{\theta}')\mathbf{H} \tag{15}$$

and so

$$\mathbf{R}(\boldsymbol{\theta}')\mathbf{E} = \mathbf{Z}'\mathbf{R}(\boldsymbol{\theta}')\mathbf{H} \tag{16}$$

or, more fully,

$$\mathbf{R}(\boldsymbol{\theta}')\mathbf{E} = \begin{bmatrix} Z'xx & Z'xy \\ Z'yx & Z'yy \end{bmatrix} \mathbf{R}(\boldsymbol{\theta}')\mathbf{H} \tag{17}$$

whence

$$\mathbf{E} = \mathbf{R}(-\boldsymbol{\theta}')\mathbf{Z}'\mathbf{R}(\boldsymbol{\theta}')\mathbf{H} \tag{18}$$
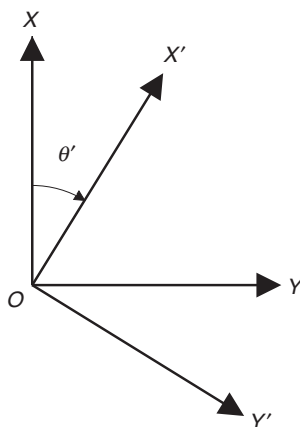

Fig. 1. The rotation of MT observing axes clockwise by angle θ', from OX and OY (north and east) to OX' and OY'.

and so

$$\mathbf{Z} = \mathbf{R}(-\boldsymbol{\theta}')\mathbf{Z}'\mathbf{R}(\boldsymbol{\theta}') \tag{19}$$

Thus the matrix $[Zxx, Zxy; Zyx, Zyy]$ upon rotation of axes changes to $[Z'xx, Z'xy; Z'yx, Z'yy]$ according to

$$\begin{bmatrix} Z'xx & Z'xy \\ Z'yx & Z'yy \end{bmatrix} = \mathbf{R}(\theta') \begin{bmatrix} Zxx & Zxy \\ Zyx & Zyy \end{bmatrix} \mathbf{R}(-\theta') \tag{20}$$

of in-phase part

$$\begin{bmatrix} Z'xx_p & Z'xy_p \\ Z'yx_p & Z'yy_p \end{bmatrix} = \mathbf{R}(\theta') \begin{bmatrix} Zxx_p & Zxy_p \\ Zyx_p & Zyy_p \end{bmatrix} \mathbf{R}(-\theta') \tag{21}$$

and quadrature part

$$\begin{bmatrix} Z'xx_q & Z'xy_q \\ Z'yx_q & Z'yy_q \end{bmatrix} = \mathbf{R}(\theta') \begin{bmatrix} Zxx_q & Zxy_q \\ Zyx_q & Zyy_q \end{bmatrix} \mathbf{R}(-\theta') \tag{22}$$

Expanding Equation 21 shows that the elements of the two matrices $\mathbf{Z}$ and $\mathbf{Z}'$ are related by the equations

$$Z'xx_p = (Zxx_p + Zyy_p)/2 + C_p\sin(2\theta' + \beta_p) \tag{23}$$

$$Z'xy_p = (Zxy_p - Zyx_p)/2 + C_p\cos(2\theta' + \beta_p) \tag{24}$$

$$Z'yx_p = -(Zxy_p - Zyx_p)/2 + C_p\cos(2\theta' + \beta_p) \tag{25}$$

$$Z'yy_p = (Zxx_p + Zyy_p)/2 - C_p\sin(2\theta' + \beta_p) \tag{26}$$

where

$$C_p = \frac{1}{2}\left[(Zxx_p - Zyy_p)^2 + (Zxy_p + Zyx_p)^2\right]^{\frac{1}{2}} \tag{27}$$

(taking the positive square root) and β_p is defined by

$$\tan\beta_p = (Zxx_p - Zyy_p)/(Zxy_p + Zyx_p) \tag{28}$$

It is also useful to define an angle μ_p as

$$\tan\mu_p = (Zyy_p + Zxx_p)/(Zxy_p - Zyx_p) \tag{29}$$

and a (positive) quantity Z_p^L as

$$Z_p^L = \frac{1}{2}\left[(Zxx_p + Zyy_p)^2 + (Zxy_p - Zyx_p)^2\right]^{\frac{1}{2}} \tag{30}$$

with an auxiliary angle $\beta_p{}'$ as

$$\tan\beta_p' = (Z'xx_p - Z'yy_p)/(Z'xy_p + Z'yx_p) \tag{31}$$

The angles β_p, μ_p and $\beta_p{}'$ may all be determined with a range of $360°$. Then

$$\theta' = (\beta_p' - \beta_p)/2 \tag{32}$$

Note that $(Z'xx_p + Z'yy_p)$, $(Z'xy_p - Z'yx_p)$, C_p and Z_p^L are independent of θ', and so are 'rotational invariants'.

Expanding Equation 22 in the same way as Equation 21 produces for the quadrature part of the tensor a set of equations just like 23 to 32, with subscript q replacing subscript p. Then $(Z'xx_q + Z'yy_q)$, $(Z'xy_q - Zyx_q)$, C_q and Z_q^L are also seen to be independent of θ', and so also are rotational invariants.

The depiction of MT tensors using Mohr diagrams

The general case: 3D structure

It can be seen from Equations 23 and 24 that plotting $Z'xx_p$ against $Z'xy_p$ as the axes are rotated (i.e. θ' varies) defines a circle, known (with its axes) as a Mohr diagram. An example is shown in

Figure 2a, for the general case of 3D conductivity structure. For the in-phase case, the centre of the circle is at the point $[(Zxy_p - Zyx_p)/2, (Zxx_p + Zyy_p)/2]$ and the radius of the circle is C_p. Different points on the diagram can be checked to confirm that Equations 23 to 32 for the rotation of axes are obeyed. Figure 2a further shows how axes for $Z'yx_p$ and $Z'yy_p$ may be included on the diagram, to display the variation of these components also.

Following the same procedure for the quadrature part of an MT tensor produces a similar Mohr diagram, and diagrams for in-phase and quadrature data may be presented as adjacent figures. Such pairs are shown in Figure 2b, c, which also draws attention to the particular cases of 2D and 1D conductivity structure to which the 3D case simplifies.

When axes for $Z'yx_p$ and $Z'yy_p$ are included it is clear to see why the phase of Zxy (as the arctangent of the ratio Zxy_q/Zxy_p of two evidently positive quantities Zxy_q and Zxy_p) is commonly in the range 0° to 90°, and the phase of Zyx (as the arctangent of the ratio Zyx_q/Zyx_p of two evidently negative quantities Zyx_q and Zyx_p) is commonly in the range 180° to 270° (or equivalently –180° to –90°).
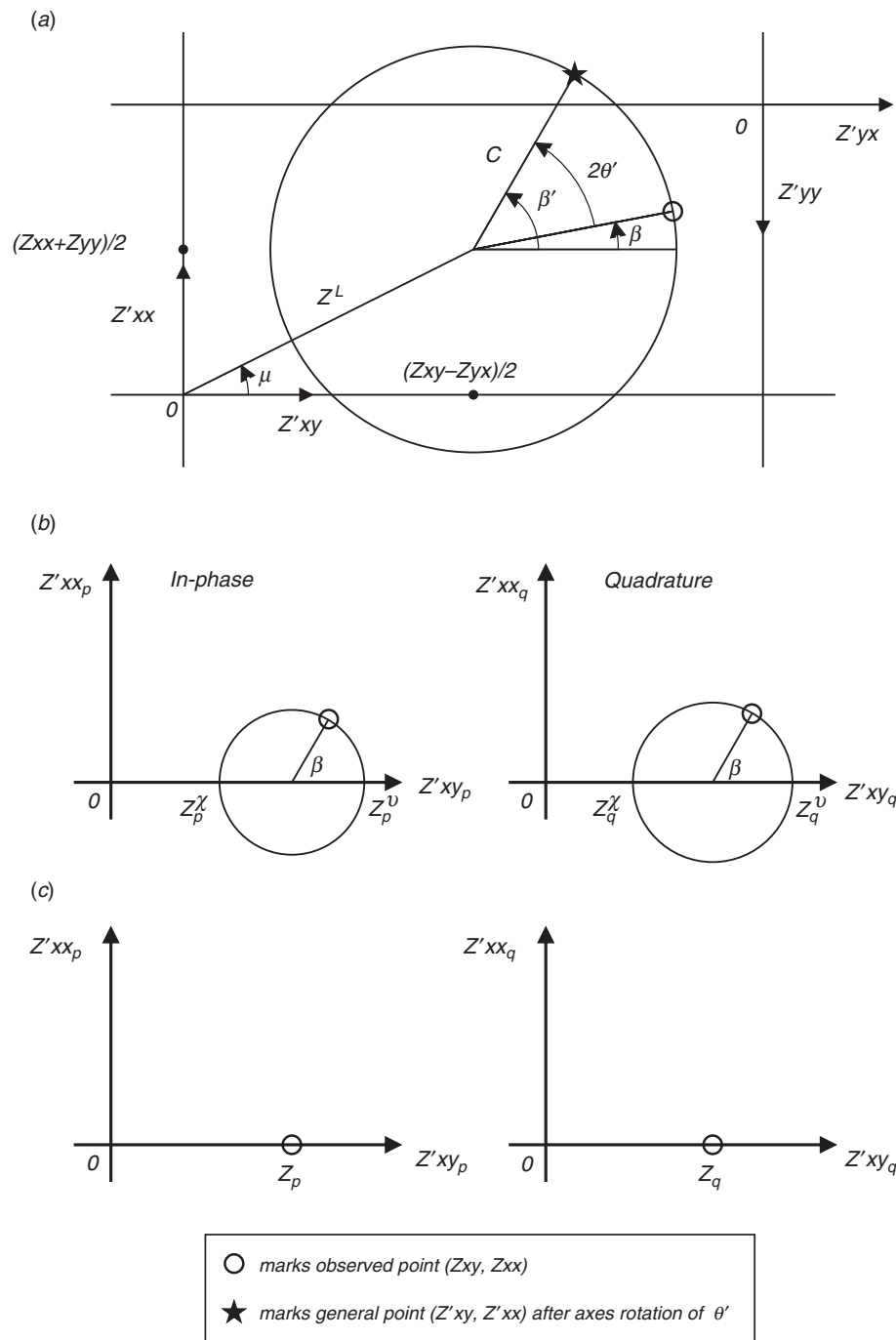

Fig. 2. (a) A Mohr diagram, typical of both the in-phase and quadrature parts of an MT tensor. Add a subscript p to every quantity shown to get a diagram for the general form of the in-phase part of the tensor, or add a subscript q to every quantity shown to get a diagram for the general form of the quadrature part of the tensor. (b) The 2D case; radial arms for the in-phase and quadrature parts of the tensor are now parallel, with both circle centres on the horizontal axes. (c) The 1D case, for $\mathbf{Z}$ observed as $[0, Z; –Z, 0]$. The circles have contracted to their central points.

2D structure

When the geologic structure is 2D and the axes are rotated to be along and across geologic strike, the rotated MT tensor will have the form $[0, Z^v; -Z^\chi, 0]$ where it is expected that all of Z^v_p, Z^v_q, Z^χ_p and Z^χ_q will be positive.

At that rotation the terms $Z'xx_p$ and $Z'yy_p$ in Equations 23 and 26 are both then zero. This circumstance produces two demands, firstly that

$$Zxx_p + Zyy_p = 0 \qquad (33)$$

with the consequence that the centre of the Mohr circle lies on the $Z'xy_p$ axis, and secondly that

$$C_p \sin(2\theta' + \beta_p) = 0 \qquad (34)$$

For non-zero C_p there are thus two solutions for θ', notably

$$2\theta' + \beta_p = 0, \pi \qquad (35)$$

i.e.

$$\theta' = -\beta_p/2, (\pi/2 - \beta_p/2) \qquad (36)$$

There is thus an ambiguity of 90° in the determination of angle θ', which (see Figure 1) is now the strike angle, relative to the initial observing axes.

The same procedure as described so far in this section may be followed for the quadrature part of an MT tensor, to produce a set of equations like Equations 33 to 36 with subscript p replaced by subscript q. Then as shown in Figure 2b, the diagram becomes a pair of circles with origins on the $Z'xy_p$ and $Z'xy_q$ axes; angles μ_p and μ_q are zero. Because for 2D the in-phase and quadrature strike directions are the same,

$$\beta_p = \beta_q \qquad (37)$$

and the in-phase and quadrature radial arms are parallel.

Z^v and Z^χ are described as the *TE* and *TM* (or vice-versa) modes of 2D induction, where *TE* stands for 'transverse electric' and *TM* stands for 'transverse magnetic'. These modes are also sometimes called *E–pol* and *B–pol* respectively, for 'E-polarisation' and 'B-polarisation'.

1D structure

If a 2D case simplifies further to become a 1D case, then $Z^v = Z^\chi = Z$ say, and the tensor for all rotations has the form $[0, Z; -Z, 0]$, where Z_p and Z_q are both positive. With reference to Equations 24 and 25, the terms $Z'xy_p$ and $Z'yx_p$ must be constant for varying θ', demanding that

$$C_p = 0 \qquad (38)$$

Because the lengths of the two radial arms thus vanish, the diagram reduces to a pair of points on the horizontal axes, as shown in Figure 2c.

'Singularity' of a tensor

A tensor is said to be singular when it has a determinant of zero, and cannot be inverted (Strang, 2003). Mohr diagrams display this situation clearly: when the determinant is zero, the circle will go through the origin of axes (in Figure 2a, $Z^L = C$). With a further construction which may be added to Figure 2a, a Mohr diagram also shows the determinant quantitatively (Lilley, 2016: 96).

As can be seen from inspection of Figure 2 generally, it is possible for 3D and 2D cases to be singular, but not 1D cases. The condition of singularity may be thought of as the extreme limit of anisotropy in a tensor (whether 2D or 3D).

Application of a matrix method similar to SVD

Where as Equations 13, 17 and 20 involve rotating the **E** and **H** axes together, the reduction of the observed tensor to a 2D form may be achieved by rotating the **E** and **H** axes separately. The rotations are by angles θe_p and θh_p respectively for the in-phase part of the tensor, and by angles θe_q and θh_q respectively for the quadrature part of the tensor. Each procedure is very similar to traditional singular value decomposition (Strang, 2003), but in both cases the relevant 2×2 matrix is anti-diagonalised, rather than diagonalised.

Thus, taking the **H** field to be completely in-phase, solutions are sought for

$$\boldsymbol{R}(\theta e_p)\mathbf{E}_p = \begin{bmatrix} 0 & \Upsilon_p \\ -\Psi_p & 0 \end{bmatrix} \boldsymbol{R}(\theta h_p)\mathbf{H} \qquad (39)$$

and

$$\boldsymbol{R}(\theta e_q)\mathbf{E}_q = \begin{bmatrix} 0 & \Upsilon_q \\ -\Psi_q & 0 \end{bmatrix} \boldsymbol{R}(\theta h_q)\mathbf{H} \qquad (40)$$

where it is instructive to compare the form of these equations with Equation 17.

Equation 39 may be expressed as

$$\mathbf{E}_p = \boldsymbol{R}(-\theta e_p)\begin{bmatrix} 0 & \Upsilon_p \\ -\Psi_p & 0 \end{bmatrix} \boldsymbol{R}(\theta h_p)\mathbf{H} \qquad (41)$$

and Equation 40 expressed as

$$\mathbf{E}_q = \boldsymbol{R}(-\theta e_q)\begin{bmatrix} 0 & \Upsilon_q \\ -\Psi_q & 0 \end{bmatrix} \boldsymbol{R}(\theta h_q)\mathbf{H} \qquad (42)$$

From Equation 41 the in-phase part of the tensor, $\boldsymbol{Z}_p$, is factored into

$$\begin{bmatrix} Zxx_p & Zxy_p \\ Zyx_p & Zyy_p \end{bmatrix} = \boldsymbol{R}(-\theta e_p)\begin{bmatrix} 0 & \Upsilon_p \\ -\Psi_p & 0 \end{bmatrix} \boldsymbol{R}(\theta h_p) \qquad (43)$$

and from Equation 42 the quadrature part is factored into

$$\begin{bmatrix} Zxx_q & Zxy_q \\ Zyx_q & Zyy_q \end{bmatrix} = \boldsymbol{R}(-\theta e_q)\begin{bmatrix} 0 & \Upsilon_q \\ -\Psi_p & 0 \end{bmatrix} \boldsymbol{R}(\theta h_q) \qquad (44)$$

Again, it is instructive to compare Equations 43 and 44 with Equation 20.

The four components of Equation 43 may now be solved for the four unknown quantities θe_p, θh_p, Υ_p and Ψ_p to yield:

$$\theta e_p = \frac{1}{2}\left[\arctan\frac{Zyy_p - Zxx_p}{Zxy_p + Zyx_p} + \arctan\frac{Zyy_p + Zxx_p}{Zxy_p - Zyx_p}\right] \qquad (45)$$

$$\theta h_p = \frac{1}{2}\left[\arctan\frac{Zyy_p - Zxx_p}{Zxy_p + Zyx_p} - \arctan\frac{Zyy_p + Zxx_p}{Zxy_p - Zyx_p}\right] \qquad (46)$$

$$\Upsilon_p - \Psi_p = \cos(\theta e_p + \theta h_p)[(Zxy_p + Zyx_p) \\ -\tan(\theta e_p + \theta h_p)(Zxx_p - Zyy_p)] \qquad (47)$$

and

$$\Upsilon_p + \Psi_p = \cos(\theta e_p - \theta h_p)[(Zxy_p - Zyx_p) \\ +\tan(\theta e_p - \theta h_p)(Zxx_p + Zyy_p)] \qquad (48)$$

Similarly Equation 44 may be solved to give an equivalent set of solutions for the quadrature part of a tensor: the quantities

θe_q, θh_q, Υ_q and Ψ_q are given by Equations 45, 46, 47 and 48 with subscript p replaced by subscript q. The quantities Υ_p, Υ_q, Ψ_p and Ψ_q are here termed 'principal values'.

Note that Equations 29, 45 and 46 give

$$\mu_p = \theta e_p - \theta h_p \tag{49}$$

and Equations 28, 45 and 46 give

$$\beta_p = -(\theta e_p + \theta h_p) \tag{50}$$

Equations 30, 45, 46 and 48 give

$$Z_p^L = (\Upsilon_p + \Psi_p)/2 \tag{51}$$

and Equations 27, 45, 46 and 47 give

$$C_p = (\Upsilon_p - \Psi_p)/2 \tag{52}$$

The quantities μ_p, β_p, Z_p^L and C_p in Figure 2 are thus related to the quantities which arise in the SVD analysis, and a Mohr diagram is seen to also display the SVD results of the present section.

An example which illustrates this point and uses the equivalent notations is shown in Figure 3. The figure has been drawn for the tensor (with all real components)

$$Z_p = [-1, 7; -4, 3] \tag{53}$$

The values of θe_p, θh_p, Υ_p and Ψ_p evaluated by Equations 45 to 48 above are 31.7°, 21.4°, 8.09 and 3.09 respectively. As a tutorial exercise, these values may also be read graphically off the figure.

While the use of Equations 45 to 48 should be straightforward to determine the quantities θe_p, θh_p, Υ_p and Ψ_p (and similarly θe_q, θh_q, Υ_q and Ψ_q) it is possible also to use a standard SVD algorithm, and adapt the results to give the desired quantities. Lilley (2012) discusses the results given if a matrix such as that of Equation 53 is put into a standard SVD computing routine.

Thus by rotation of the electric and magnetic axes separately, the example MT tensor has been reduced to an ideal 2D form. This exercise may be regarded as a standard SVD but adjusted to anti-diagonalise, rather than diagonalise the matrix.

In a search for the nearest 2D model in a 3D situation the results thus obtained may be valuable to bear in mind. On the grounds that distortion occurs in the electric field rather than the magnetic field, the rotated magnetic axes may give a useful indication of an 'approximate 2D regional strike'. The rotated electric axes may show a dominant direction of electric field distortion.
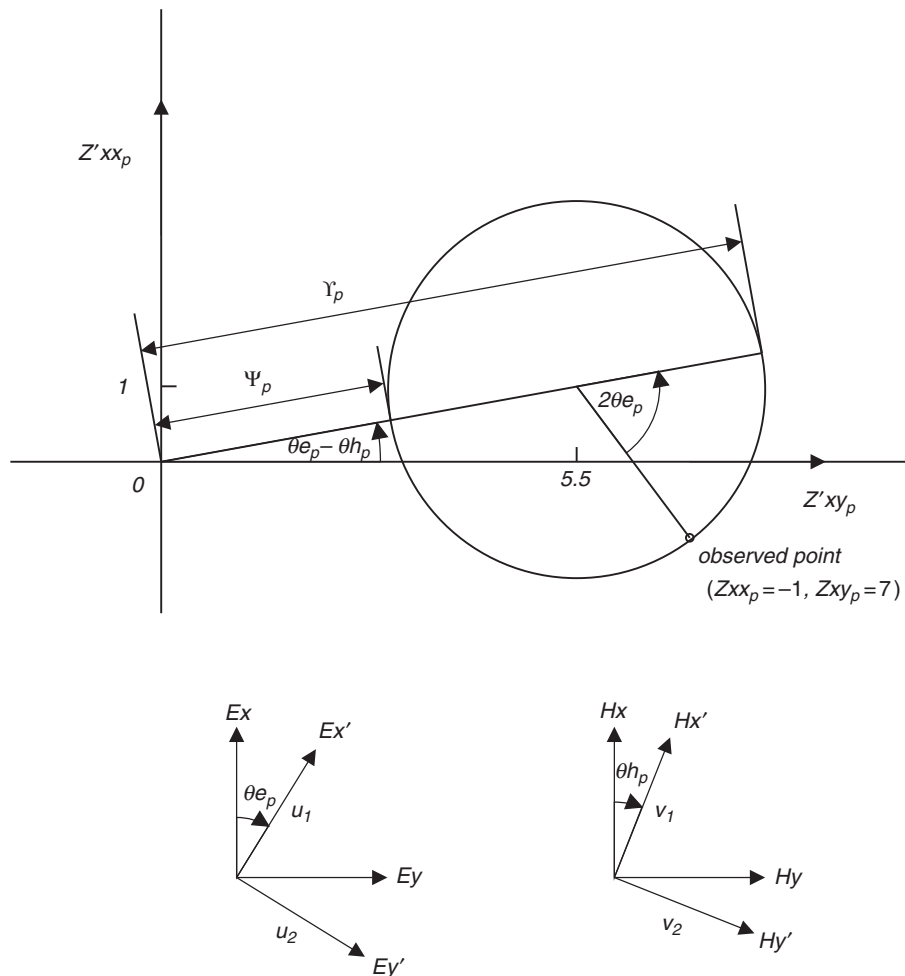

Fig. 3. Diagram showing the Mohr representation of the matrix in Equation 53, analysed by the SVD method described in the text. The values of θe_p, θh_p, Υ_p and Ψ_p are evident as 32°, 21°, 8.1 and 3.1. The axes for Ex', Ey' and Hx', Hy' show the rotations, from Ex, Ey and Hx, Hy by θe_p and θh_p respectively, to give an ideal 2D anti-diagonal response. The angle $(\theta e_p - \theta h_p)$ is termed the 'twist' of the electric-field axes relative to the magnetic-field axes.

Invariants of rotation

Many of the quantities arising so far are invariant with the rotation of the observing axes. In Figure 4 it is shown how, by inspection, an MT tensor can be expressed in terms of seven such invariants. This figure shows two figures of the form of Figure 2a juxtaposed, the left-hand one for the in-phase MT data, and the right-hand one for the quadrature MT data. Clearly λ_p, μ_p and Z_p^L are independent of λ_q, μ_q and Z_q^L, to the extent that the in-phase and quadrature parts of an MT tensor are determined independently. Also all of λ_p, μ_p, Z_p^L, λ_q, μ_q and Z_q^L are independent of θ', and so are invariants of axes rotation.

The seventh invariant shown, $\delta\beta$, can be seen to also be independent of θ' because as θ' changes the radial arms of both circles rotate together. The angle between the two radial arms ($\delta\beta$) is constant and thus is also an invariant of rotation. In this paper, $\delta\beta$ is defined as

$$\delta\beta = \beta_q - \beta_p \tag{54}$$

There are a number of different practical invariants in MT (Berdichevsky and Dimitriev, 1976; Ingham, 1988; Szarka and Menvielle, 1997; Weaver et al., 2000). The use of such invariants for dimensionality analysis has been developed especially by Marti et al. (2005, 2009, 2010) and Marti (2014); see also Jones (2012). This paper will focus on the seven invariants shown in Figure 4 and others closely related to them, and discuss the useful information they convey. Thus the eight elements of an MT tensor, all of which generally change upon axes rotation, are expressed as seven invariants of rotation plus just one quantity which does vary as the axes are rotated. As an example of the latter, the angle β in Figure 2a defines the 'observed point', and the tensor element values at this point in turn respond to the directions of the measuring axes.

The set of invariants given in Figure 4 will now be reviewed.

Two invariants summarising the 1D character of the tensor

The two invariants Z_p^L and Z_q^L summarising the 1D character are straightforward and were termed 'central impedances' by Lilley (1993). For graphical representation it may be convenient to multiply them by $T^{1/2}$, in view of the common tendency of tensor elements to show a period dependency of $T^{-1/2}$ (see *Units of E, Z and H*).

Alternatively they may be combined as per Equations 10 and 11 and presented as values of apparent resistivity (ρ_{aZ^L}) and phase (ϕ_{Z^L}), computed as

$$\rho_{aZ^L} = \frac{1}{\omega\mu}\left(Z_p^{L2} + Z_q^{L2}\right) \tag{55}$$

and

$$\phi_{Z^L} = \arctan\left(\frac{Z_q^L}{Z_p^L}\right) \tag{56}$$

An example of this presentation will be given below in Figure 9.

Two invariants summarising the 2D character of the tensor

Two invariants λ_p and λ_q measure the 2D character of the MT tensor, and are also straightforward. They are naturally angles, and were termed anisotropy angles by Lilley (1993). With reference also to Figure 2a they may be expressed

$$\lambda_p = arcsin(C_p/Z_p^L) \tag{57}$$

and

$$\lambda_q = arcsin(C_q/Z_q^L) \tag{58}$$

where λ_p and λ_q are both in the range 0 to 90°. Note this definition fails if either $C_p > Z_p^L$ or $C_q > Z_q^L$ (or both), and the relevant circle encloses its origin of axes.

The special cases $\lambda_p = 0$ and $\lambda_q = 0$ arise when the data show nil 2D characteristics. The data are then either pure 1D; or 'twisted 1D' (Lilley, 1993), and so 3D.

The special cases $\lambda_p = 90°$ and $\lambda_q = 90°$ arise when the in-phase and quadrature parts respectively of the tensor are so anisotropic as to be singular. Thus a value of λ_p and λ_q near 90° indicates that a condition of singularity is being approached.

Two (of three) invariants summarising the 3D character of the tensor

The two angles μ_p and μ_q shown in Figure 4 characterise the 3D nature of the impedance tensor and are also straightforward. It may be useful to express them as their mean and difference values (this practice is adopted in the example below) because certain mechanisms for causing 3D effects, notably those with a strong twist component, give similar μ contributions to both the in-phase and quadrature parts of a tensor (Lilley, 1993). In cases of the distortion of a regional 2D structure by a 'twist' factor only, the twist is then measured by $(\mu_p + \mu_q)/2$ and the difference $(\mu_q - \mu_p)$ should be zero.
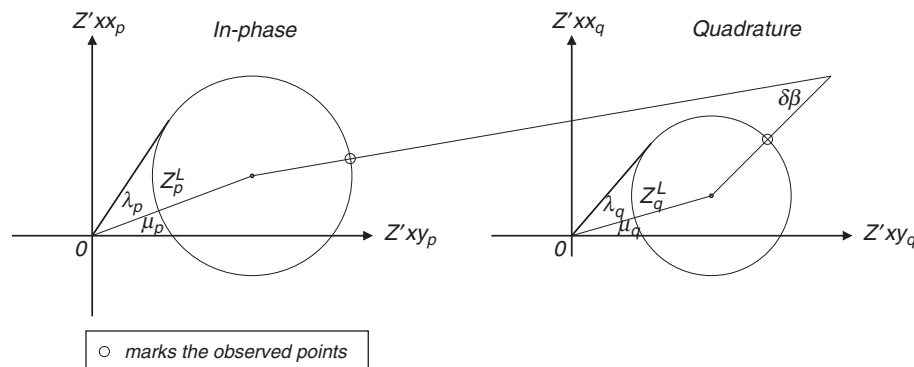

Fig. 4. Seven invariants of rotation for a general 3D MT tensor. Two invariants Z_p^L and Z_q^L (in the units of the tensor elements) measure 1D characteristics. Two angles λ_p and λ_q measure 2D characteristics. Three angles μ_p, μ_q and $\delta\beta$ measure 3D characteristics.

The third 3D invariant: the '7th invariant'

The third 3D invariant shown in Figure 4, $\delta\beta$, can be seen to be the angle by which the two radial arms of the in-phase and quadrature circles are not parallel. It is significant as of the invariants shown in Figure 4, it alone links the in-phase and quadrature parts of an observed tensor. Care must be taken with its sign (see Equation 54). This '7th invariant' and other invariants closely related to it will be discussed further below.

The invariants of Bahr (1988) and Weaver et al. (2000)

This paper will shortly introduce a 7th invariant which is developed from the $\delta\beta$ of Figure 4, and is used below in place of the 7th invariant of Weaver et al. (2000). As context, it is necessary to first summarise both the analysis of Bahr (1988), and also the 'WAL2000' analysis of Weaver et al. (2000). The reason is that the 7th invariant of WAL2000 is closely linked to the Bahr analysis.

The Bahr (1988) analysis

In this important and pioneering model of tensor distortion, Bahr first notes that if a regional 2D tensor with an unknown (but defined) strike is distorted by a (purely in-phase) tensor d according to

$$Z = \begin{bmatrix} d_1 & d_2 \\ d_3 & d_4 \end{bmatrix} Z_{2D} \qquad (59)$$

where Z_{2D} has the form $[0, Z'; -Z^x, 0]$, then

$$Z = \begin{bmatrix} -d_2 Z^x & d_1 Z^v \\ -d_4 Z^x & d_3 Z^v \end{bmatrix} \qquad (60)$$

when the measuring axes are aligned with the regional strike.

When, as in the general case, the measuring axes are not aligned with the regional strike, there will be an angle α for measuring-axes rotation at which a magnetic signal in the $H'x$ direction will give an electric field signal $(Z'xx\,H'x\,\hat{x}' + Z'yx\,H'x\,\hat{y}')$ which is linearly polarised. At that rotation, the measuring axes will be aligned with the regional strike.

That is, the phases of $Z'xx\,H'x$ and $Z'yx\,H'x$ must be the same, and so the phases of $Z'xx$ and $Z'yx$ must be the same. Thus

$$\frac{Z'xx_q}{Z'xx_p} = \frac{Z'yx_q}{Z'yx_p} \qquad (61)$$

and Equation 61 can be used to find a solution for α. In fact two solutions for α will be found, and in the (ideal) case of Equation 59 they will differ by 90°.

However values of rotation angle α which give the 'equal phase' condition of Equation 61 can be sought for any observed MT tensor. Call two such solutions α_1 and α_2, and in this paper both are defined in the range $0 \leq \alpha < 180°$, with $\alpha_2 > \alpha_1$.

For the ideal case of Equation 59 the two α values differ by 90°. Thus the closer the difference between the two α values now found is to 90°, the closer the actual MT situation is to the ideal model. At best, two such values found for α will give the direction of a 2D regional geologic strike (with a 90° ambiguity).

Bahr (1988, 1991) further defines a 'phase-sensitive' skew value η as an 'ad hoc' measure of the departure from his model of data being fitted to it. Such values for η are included in the example of MT data given below. For the mathematical derivation of η the interested reader is referred to the papers cited, and see also Simpson and Bahr (2005). For an η value of zero the regional structure is indeed 2D, the data conform to

Equation 59, and again the strike is given, with a 90° ambiguity, by either α_1 or α_2 (which now differ by 90° exactly).

In the general case where the equal-phase condition of Equation 61 is met for axes rotation α_1, an angular deviation ξ_1 of the telluric field in the y' direction occurs such that

$$\tan\xi_1 = -\frac{Z'xx_p}{Z'yx_p} \qquad (62)$$

and also

$$\tan\xi_1 = -\frac{Z'xx_q}{Z'yx_q} \qquad (63)$$

Similarly for axes rotation α_2, with correspondingly different values of $[Z'xx, Z'xy; Z'yx, Z'yy]$, an angular deviation ξ_2 occurs such that

$$\tan\xi_2 = -\frac{Z'xx_p}{Z'yx_p} \qquad (64)$$

and also

$$\tan\xi_2 = -\frac{Z'xx_q}{Z'yx_q} \qquad (65)$$

The Bahr analysis can be displayed on a Mohr diagram, as shown in Figure 5 for the example data NQ101R at period $T = 0.0353$ s. At this period, two solutions for α have indeed been found ($\alpha_1 = 46.1°$ and $\alpha_2 = 139.9°$). The upper part of Figure 5 is reproduced in Appendix A in more detail. It can be seen that $(\pi - \alpha_2 + \alpha_1)$ is indeed close to 90°, and thus α_2 is indeed close to $(\alpha_1 + 90°)$.

For many MT data, however, solutions for α_1 and α_2 will not be found, consistent with a condition given by Bahr (1988) not being met. For the example data presented below, as the graphs there will show, only for parts of the data spectrum is the condition satisfied and angles α_1 and α_2 found.

The set I_1, I_2, I_3, I_4, I_5, I_6 and I_7 of Weaver et al. (2000)

The first six of the set of invariants of Weaver et al. (2000) follow the set of invariants of Lilley (1998) and comprise the Z_p^L, Z_q^L, λ_p, λ_q, μ_p and μ_q of Figure 4, with the changes that sines of angles are taken rather than the angles themselves. Thus Z_p^L is taken as I_1 and Z_q^L is taken as I_2, but $\sin\lambda_p$ (rather than λ_p) is taken as I_3, and $\sin\lambda_q$ (rather than λ_q) is taken as I_4.

Further, rather than taking μ_p and μ_q individually, their sum $(\mu_p + \mu_q)$ and difference $(\mu_q - \mu_p)$ are taken. Then, again taking sines rather than basic angle values, WAL2000 define $\sin(\mu_p + \mu_q)$ as I_5 and $\sin(\mu_q - \mu_p)$ as I_6.

Taking the sines of angles is intended to produce values with magnitudes on the convenient scale of 0 to 1, but this procedure does not allow for angles greater than 90° without introducing ambiguity in interpretation, because $\sin(\pi - \mu) = \sin\mu$. While the values of λ_p and λ_q will never exceed 90°, in cases of strong distortion the values of μ_p and μ_q may exceed 45° so that the value of $(\mu_p + \mu_q)$ may indeed exceed 90°. Cases of such strong distortion are not uncommon, and thus the use of actual angle values (rather than taking their sines) is followed generally in the present paper.

The seventh invariant of WAL2000, denoted I_7, is not the obvious $\delta\beta$ from Figure 5, but rather is based on the ideal galvanic distortion model of Bahr. In terms of the Bahr model described above, the WAL2000 I_7 has the value

$$I_7 = \sin(\alpha_2 - \alpha_1 - \pi/2) \qquad (66)$$

and may be demonstrated graphically by a construction added to Figure 5, as discussed in Appendix A below.

Weaver et al. (2000) also show that their I_7 is related to $\delta\beta$ (using the notation of Figure 4 of the present paper) by

$$I_7 = \frac{\sin(\mu_q - \mu_p) - \sin\lambda_p \sin\lambda_q \sin\delta\beta}{Q} \qquad (67)$$

where the dimensionless quantity Q (also an invariant) is defined as

$$Q^2 = \sin^2\lambda_p + \sin^2\lambda_q - 2\sin\lambda_p \sin\lambda_q \cos(\mu_q - \mu_p - \delta\beta) \qquad (68)$$

Values of I_7 may thus be calculated using Equation 67 even when solutions for α_1 and α_2 do not exist and Equation 66 cannot be applied. Such values of I_7 calculated using Equation 67 are included in the section below, but note they are susceptible to instability when Q, the denominator of Equation 67, becomes small. Also, once solutions for α_1 and α_2 can no longer be found, the appeal of I_7 as being simply related to α_1 and α_2 is lost and the physical significance of I_7 becomes obscure. This situation gives rise to further enquiry regarding possible '7th' invariants.

Appendix B presents some further notes on the resolution of the slightly different definitions for the Bahr strike angles of the Bahr (1988) and Weaver et al. (2000) papers.

Invariant $\Delta\beta$, an extension of $\delta\beta$

As illustrated by Figures 3 and 4, Equations 50 and 54 give

$$\delta\beta = -\theta e_q - \theta h_q + \theta e_p + \theta h_p \qquad (69)$$

which in view of Equation 49 may be expressed

$$\delta\beta = \mu_q - \mu_p - 2(\theta e_q - \theta e_p) \qquad (70)$$

Thus, for the simplest cases where $\theta e_q = \theta e_p$, the angle $\delta\beta$ in Figure 4 will take the value of $(\mu_q - \mu_p)$, and the value of $(\mu_q - \mu_p - \delta\beta)$ will be zero.

A further invariant is thus suggested, here called $\Delta\beta$ and defined as

$$\Delta\beta = \mu_q - \mu_p - \delta\beta \qquad (71)$$

which tests whether $(\mu_q - \mu_p - \delta\beta)$ is indeed zero. When not zero, $\Delta\beta$ gives a measure of the departure of the observed tensor from the situation in which all 3D characteristics are accounted for by the quantities $(\mu_q - \mu_p)$ and $(\mu_p + \mu_q)/2$, and so more basically by μ_p and μ_q.
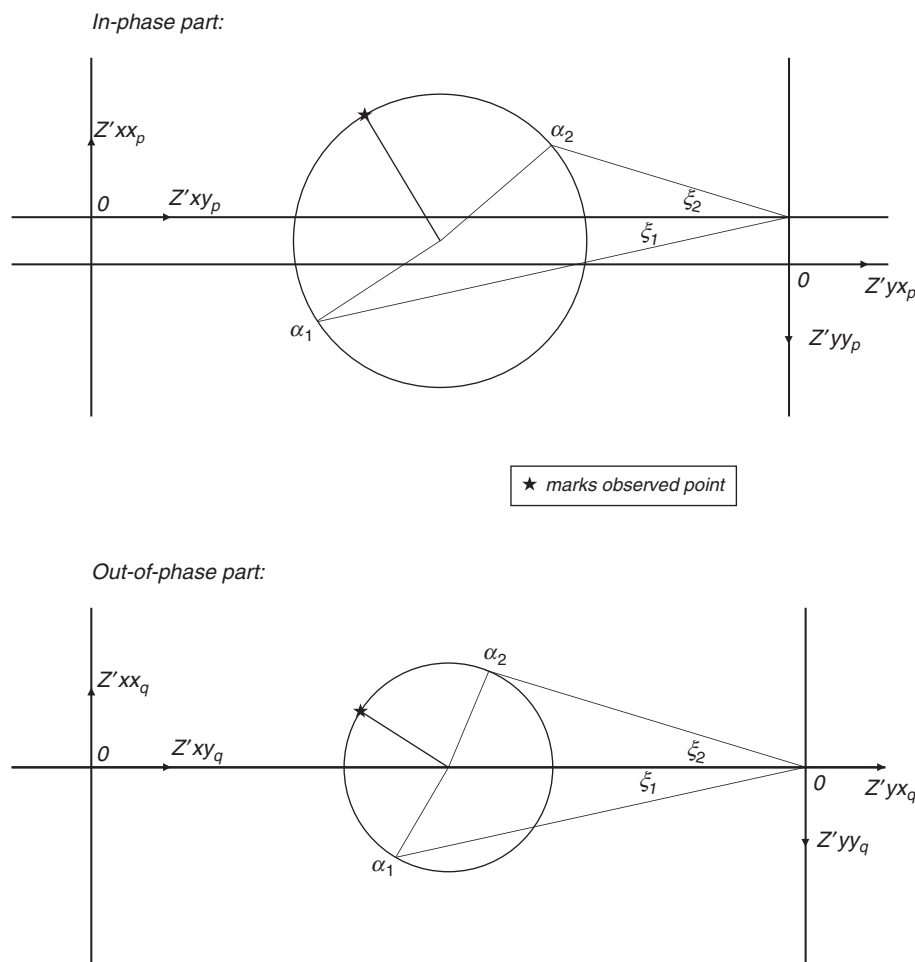

Fig. 5.   The Bahr analysis demonstrated using data from site NQ101R, $T = 0.0353$ s. Upper diagram is for the in-phase data, lower diagram is for the out-of-phase data. The angles α_1 (46.1°) and α_2 (139.9°) are the two angles for the rotation of the horizontal axes at which the Bahr decomposition applies. The angles ξ_1 (–12.4°) and ξ_2 (16.9°) are then the Bahr distortion angles, common for both the in-phase and quadrature data. See Appendix A for more details regarding angles α_1 and α_2.

Note further that $\Delta\beta$ is the angle which occurs in the cosine factor in Equation 68. Also, that by Equations 70 and 71, $\Delta\beta$ can be expressed in the simple form:

$$\Delta\beta = 2(\theta e_q - \theta e_p) \qquad (72)$$

It is a condition of 2D cases that $\theta e_q = \theta e_p$, (see Figures 2 and 3). Thus $\Delta\beta = 0$ is the case automatically in all 2D cases, whether or not the anisotropy is strong.

But note that $\Delta\beta$ will also become small and approach zero in 3D cases where there is a strongly dominant direction of electric field signal, for which $\theta e_q \approx \theta e_p$. This situation may occur in 3D cases where, for example, the MT tensor approaches singularity in both its in-phase and quadrature parts, due to strong distortion by a pure-real tensor.

For completeness it should be added that, for 1D cases, θe_p and θe_q do not exist (see Figures 2 and 3), and $\Delta\beta$ is not defined.

$\Delta\beta$ and Q

Equation 68 for Q may be displayed as the geometric relationship shown in Figure 6. In Figure 6b, the angle $\Delta\beta$ is now seen to have a major influence in controlling the magnitude of Q. It is evident that Q has the range $0 \leq Q \leq 2$, and that to minimise Q the value of $(\mu_q - \mu_p - \delta\beta)$ must be zero. Study of Figure 6 makes clear the further condition required for $Q = 0$, that $\lambda_p = \lambda_q$.

The condition $Q = 0$ thus requires that both the in-phase and the quadrature parts of an MT tensor have the same 2D measure, i.e. that $\lambda_p = \lambda_q$, and also the same 3D measures, i.e. that $\mu_q - \mu_p = 0$. The condition $Q = 0$ further requires that $\beta_q - \beta_p = 0$. The condition $Q = 0$ is thus met only by one particular and highly restricted class of 3D (and 2D) structures, though note that there is a special case possible for $Q = 0$ in which $(\mu_q - \mu_p) - (\beta_q - \beta_p) = 0$ but $\mu_q - \mu_p \neq 0$ and $\beta_q - \beta_p \neq 0$, with $\lambda_p = \lambda_q$.

The quantity Q is thus comprehensive in being a function of both the 2D and the 3D measures of an MT tensor. However it is just this very property, of showing a combined 2D and 3D response, that causes Q to be a less appropriate '7th' invariant than $\Delta\beta$. Non-zero values of $\Delta\beta$ are a function of 3D characteristics only.

Some further invariants

This section describes a number of further invariants, which will be compared for the characteristics they show in the analysis of field data.
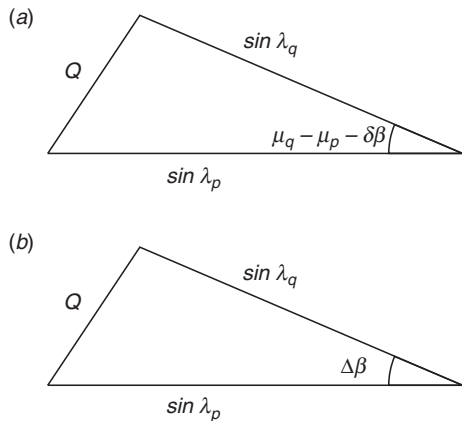

Fig. 6. (*a*) Equation 68 for Q expressed geometrically in terms of the quantities shown in Figure 4. The side of length Q is opposite the angle $(\mu_q - \mu_p - \delta\beta)$ which may thus be termed the 'Q angle'. (*b*) Equation 68 for Q expressed geometrically now with the 'Q angle' recognised as $\Delta\beta$.

Invariants $(\lambda_p + \lambda_q)/2$ and $(\lambda_q - \lambda_p)$

As noted in the section *Two invariants summarising the 2D character of the tensor*, the quantities λ_p and λ_q are both gauges of two-dimensionality. In the next section below they are presented as mean and difference values, following the practice developed for μ values.

Invariants det $\boldsymbol{Z}_p$ and det $\boldsymbol{Z}_q$

The determinants of the in-phase and quadrature parts of the MT tensor taken separately, given by

$$\det \boldsymbol{Z}_p = Zxx_p \, Zyy_p - Zxy_p \, Zyx_p \qquad (73)$$

and

$$\det \boldsymbol{Z}_q = Zxx_q \, Zyy_q - Zxy_q \, Zyx_q \qquad (74)$$

are invariants, and reduce to zero if $\boldsymbol{Z}_p$ and $\boldsymbol{Z}_q$ respectively approach conditions of singularity (Lilley, 2016: 96). They are included in the example results below multiplied by period T (and so as det $\boldsymbol{Z}_p \, T$ and det $\boldsymbol{Z}_q \, T$) to counter the common $T^{-1/2}$ period dependency of tensor element values, explained in the section *Units of E, Z and H*.

Invariants κ_p and κ_q

The quantities κ_p and κ_q are condition numbers, as defined for magnetotelluric data by Lilley (2012). In Figure 3, κ_p is given by

$$\kappa_p = \Upsilon_p / \Psi_p \qquad (75)$$

and will become large as the in-phase part of the tensor approaches the condition of singularity (and its Mohr circle approaches the origin of axes). κ_q is defined, and behaves, similarly.

Dimensionless and invariant with axes rotation, κ_p and κ_q are thus direct gauges of the in-phase and quadrature parts respectively of a tensor approaching singularity. Because they are ratios they do not depend on the absolute values of the tensor elements, as do the invariants det $\boldsymbol{Z}_p$ and det $\boldsymbol{Z}_q$.

Examples using MT data: the site 'NQ101R'

The invariants described above are now presented graphically for data from a particular Australian MT site, NQ101R, which is offered as typical of many sites. Analysis begins with the NQ101R data as tensor-element values in the practical units of mV/km/nanotesla. In the graphs in the present section, the unit of apparent resistivity is Ωm, and the unit for angles (including phase) is *degree*. The NQ101R data set has been chosen as, over the period range of observation, its characteristics change greatly, though not in an atypical way. Results for just one observing site are thus sufficient to show a wide range of significant 2D and 3D characteristics.

Thus Figure 7 shows the basic MT data, supplied as in-phase and quadrature values at different periods of the elements of [Zxx, Zxy; Zyx, Zyy], and here presented as plots of apparent resistivity (in panels A1-A4) and phase (in panels B1-B4), taking each element separately (see Equations 10 and 11). It can be seen that the situation occurs where, with increasing period, $\rho_{a\,Zyy}$ grows to be greater than $\rho_{a\,Zyx}$; and where as $\rho_{a\,Zxx}$ gets very weak, its phase goes 'out of quadrant', i.e. out of the expected range between 0° and 90°.

Panels A5 and B5 show the det $\boldsymbol{Z}_p \, T$ and det $\boldsymbol{Z}_q \, T$ determinant values reducing to near zero with increasing period, as both the in-phase and quadrature parts of the tensor approach singularity. In panels A6 and B6 the condition numbers, κ_p and κ_q, give

different measures of the same phenomenon, now with values increasing above 10 as the in-phase and quadrature parts of the tensor approach singularity.

The panels C1 and D1 show Mohr diagram presentations of the observed data, and exhibit much of the information spelled out in the other panels.

The panels C3, D3, C4 and D4 show the singular value decomposition of the tensor as outlined in the section *Application of a matrix method similar to SVD* above, where the major principal values (in-phase and quadrature) have been combined to give $\rho_{a\,ZPyx}$ (apparent resistivity) and ϕ_{ZPyx} (phase) results, as have the minor principal values to give $\rho_{a\,ZPxy}$ and ϕ_{ZPxy} results. The rotation angles for the electric field axes, θe_p and θe_q, are given in panels C5 and D5, and the rotation angles for the magnetic field axes, θh_p and θh_q, are given in panels C6 and D6. Over the whole period range the θe values (panels C5 and D5) are in good agreement, and change little. The θh values (panels C6 and D6) also are in good agreement, but are period dependent, changing through almost 90° over the period range.

On the grounds that distortion is in the electric field rather than in the magnetic field, one might look to both θh_p and θh_q as indicative of 2D strike. However the data are too 3D for a 2D model to be justified, a conclusion demonstrated particularly by the period dependence of the θh_p and θh_q results.

Figure 8 shows further invariants of the NQ101R data. Panel E1 shows the invariant I_1 of WAL2000 as determined, and panel F1 shows I_1 multiplied by $T^{1/2}$ to counter the $T^{-1/2}$ period dependency referred to above. Similarly panels G1 and H1 display I_2 which, with I_1, indicates the '1D magnitude' of the data.

Panels E2 and F2 then show the two anisotropy angles λ_p and λ_q, which measure two-dimensionality. In panels G2 and H2 the means and differences of these two angles are plotted, showing that they are similar at the start and finish of the period range, but for mid-periods they differ substantially. At the start of the period range both λ values are at their minimum, and at their closest to one-dimensionality. At long periods, especially the λ_p values approach their limit of 90°.

In panels E3 and F3 the basic measures of three-dimensionality (relative 'twist') are displayed, and in G3 and H3 the means and differences of these quantities are given. Again note that from a 2D (or 1D) start, with both μ values effectively zero, the three-dimensionality increases with period, to 'plateau' at long periods (see panel G3). As in panel H2, in panel H3 the differences between in-phase and quadrature values are greatest at mid-periods.

Panel E4 presents $\delta\beta$ and panel F4 presents I_7, the WAL2000 seventh invariant calculated using Equation 67. In exceeding the value of unity I_7 transgresses the intention of the WAL invariants to have a magnitude in the range $0 - 1$, and also it can clearly not be interpretated as the sine of an angle. Panel G4 displays the values of Q, and panel H4 the values of $\Delta\beta$, to which attention is drawn below as being of particular interest.

Panels E5 and F5 display the Bahr α values where they exist. Panel G5 displays them combined to give a 'mean strike direction', and panel H5 presents the difference between the two strike direction estimates. Panel E6 gives the Bahr η values, and panel F6 the sine of the difference of the two strike directions (i.e. the sine of the values in panel H5). The values in panel F6 may thus be compared to the I_7 values plotted in
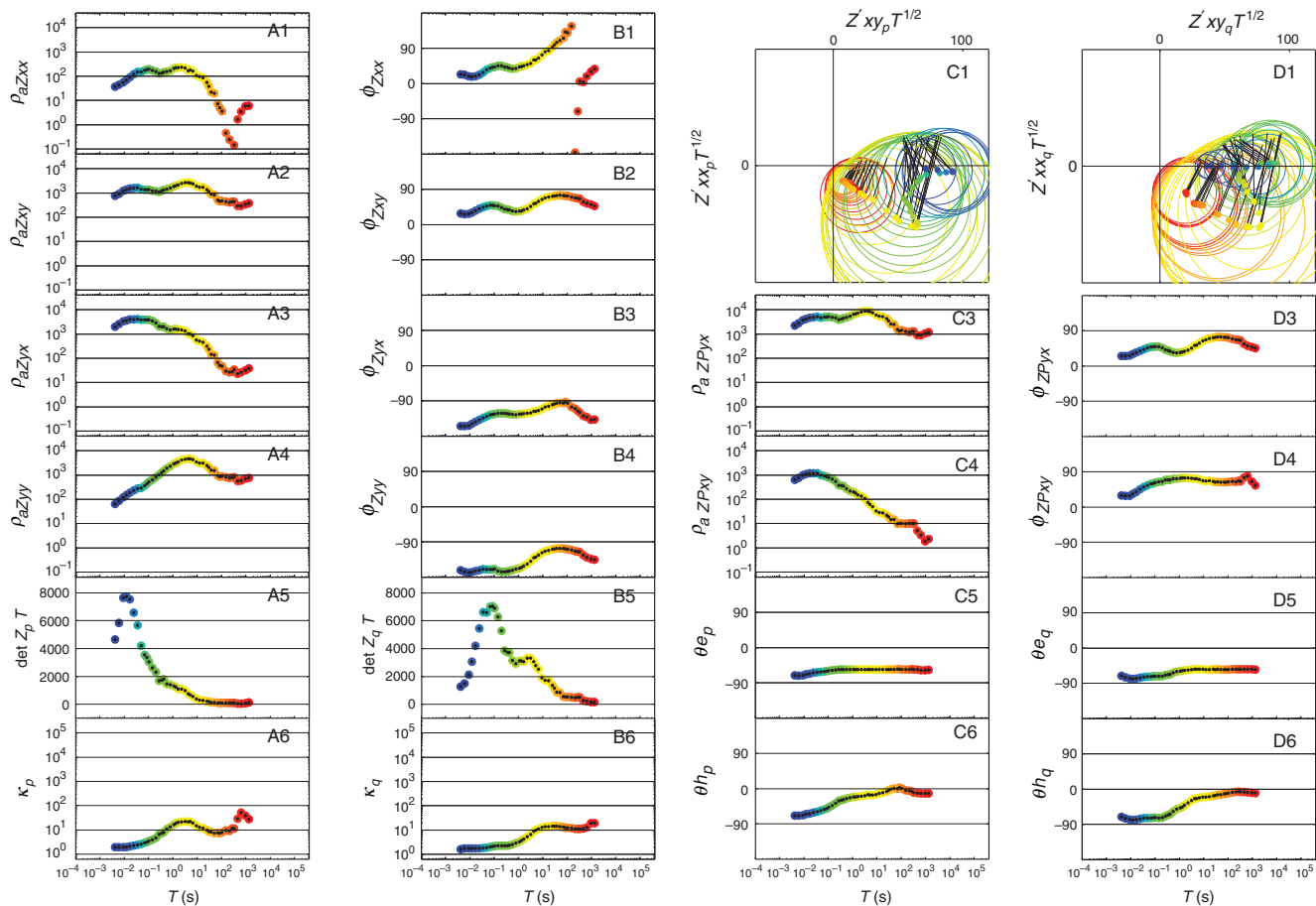

Fig. 7. Display and analysis by an SVD method of the MT data for the example site NQ101R. The data are closest to 1D at the short period (blue) end of the spectrum, where the 'near surface' apparent resistivity is of the order of 10^3 Ωm. See text for a description and discussion of the results shown.

panel F4 above, and noted to agree where values for α_1 and α_2 exist. Panels G6 and H6 then give the Bahr ξ values, where they exist.

Finally in Figure 8 panels E7 and F7 present, as mean and difference values, the θe_p and θe_q values from panels C5 and D5 of Figure 7. Consistent with Equation 72, in F7 the values taken by $(\theta e_q - \theta e_p)$ can be seen to be half those of $\Delta\beta$ as in panel H4 above. Panels G7 and H7 similarly present as mean and difference values the θh_p and θh_q values from panels C6 and D6 of Figure 7.

Remembering from Figure 6 the control of Q by the λ_p and λ_q values and by $\Delta\beta$ in particular, it can be seen in panel G4 that Q is indeed close to zero when (in panel H2) $\lambda_q \approx \lambda_p$, and (in panel H4) $\Delta\beta \approx 0$.

Discussion

Observed MT data may thus be summarised as shown for NQ101R in Figure 9. The left-hand two columns present the tensor element data in their basic form, and the right-hand two columns present the data as values of seven invariants, I'_1 to I'_7:

(i) in panel K1 the central-impedance apparent resistivity $\rho_{a Z^L}$, here called I'_1;
(ii) in panel L1 the central-impedance phase ϕ_{Z^L}, here called I'_2;

(iii) in panel K2 the mean 2D anisotropy $(\lambda_p + \lambda_q)/2$, here called I'_3;
(iv) in panel L2 the 2D anisotropy difference $(\lambda_q - \lambda_p)$, here called I'_4;
(v) in panel K3 the mean 3D 'twist' $(\mu_p + \mu_q)/2$, here called I'_5;
(vi) in panel L3 the 3D 'twist' difference $(\mu_q - \mu_p)$, here called I'_6; and
(vii) in panel K4 the 3D-sensitive Q-angle $\Delta\beta$, here called I'_7.

Panel L4 then completes the set with rotation-dependent quantity θh_p, which under certain circumstances gives an indication of geologic strike. A rotation of the horizontal measuring axes at the observing site would cause all values of θh_p to experience a zero shift. Also, from the infinite number of tensors which share the same seven invariants I'_1 to I'_7 (one tensor at every point around the circles in Figure 4), the rotation-dependent value θh_p selects the original tensor. Picking up the point of Weidelt and Chave (2012: 129), the eight values (I'_1 to I'_7 and θh_p) together allow the recovery of the original tensor in a straightforward way.

To now review Figure 9, at the short-period end of the spectrum the data are 2D, with I'_5, I'_6 and I'_7 all near zero. In fact, to the extent that I'_3 and I'_4 are also both small, the data are approximately 1D, indicating near-surface apparent resistivity and phase values as given by I'_1 and I'_2 respectively.

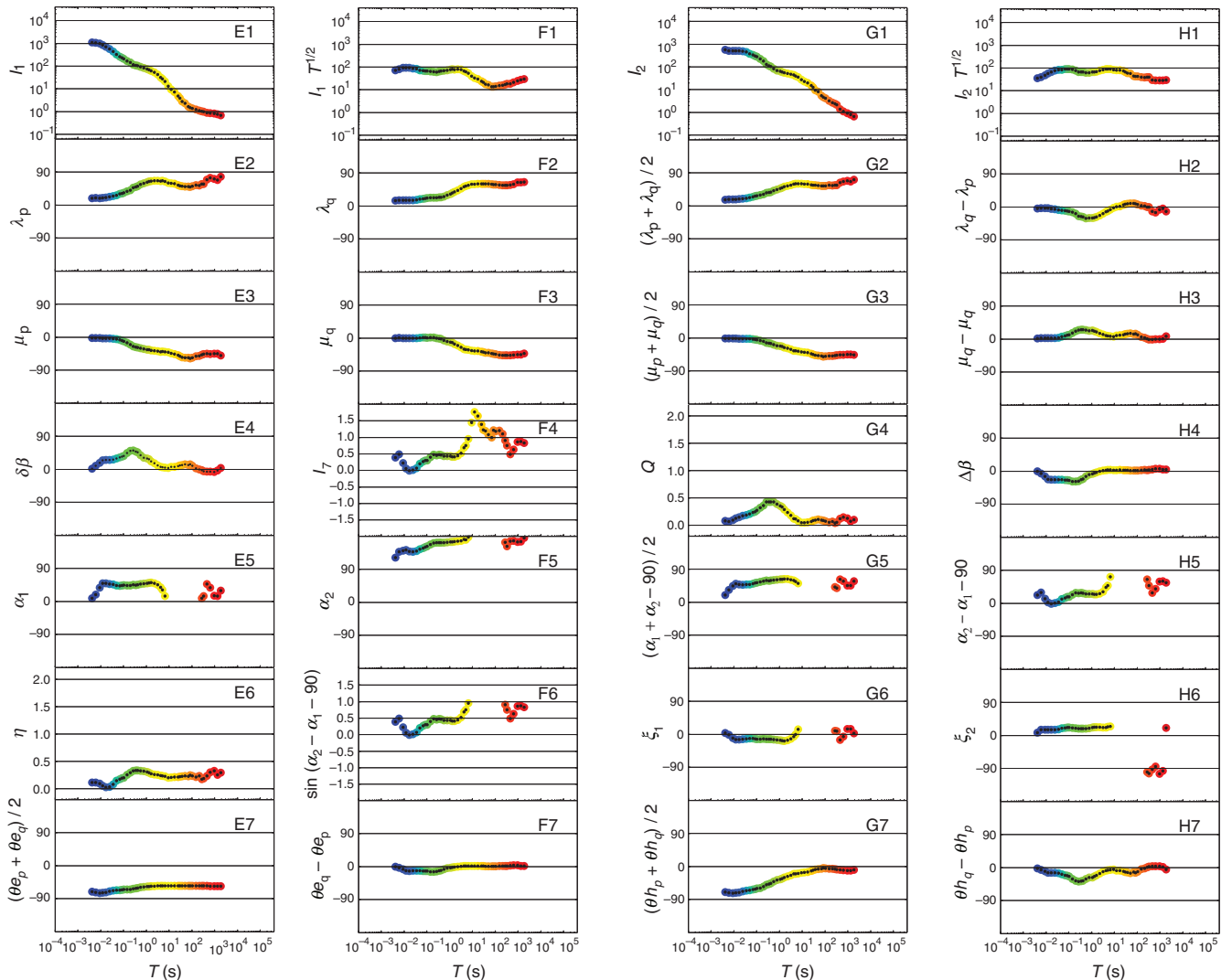**Fig. 8.** Analysis of the MT data for site NQ101R, showing the values of the invariants described and discussed in the text as functions of period.
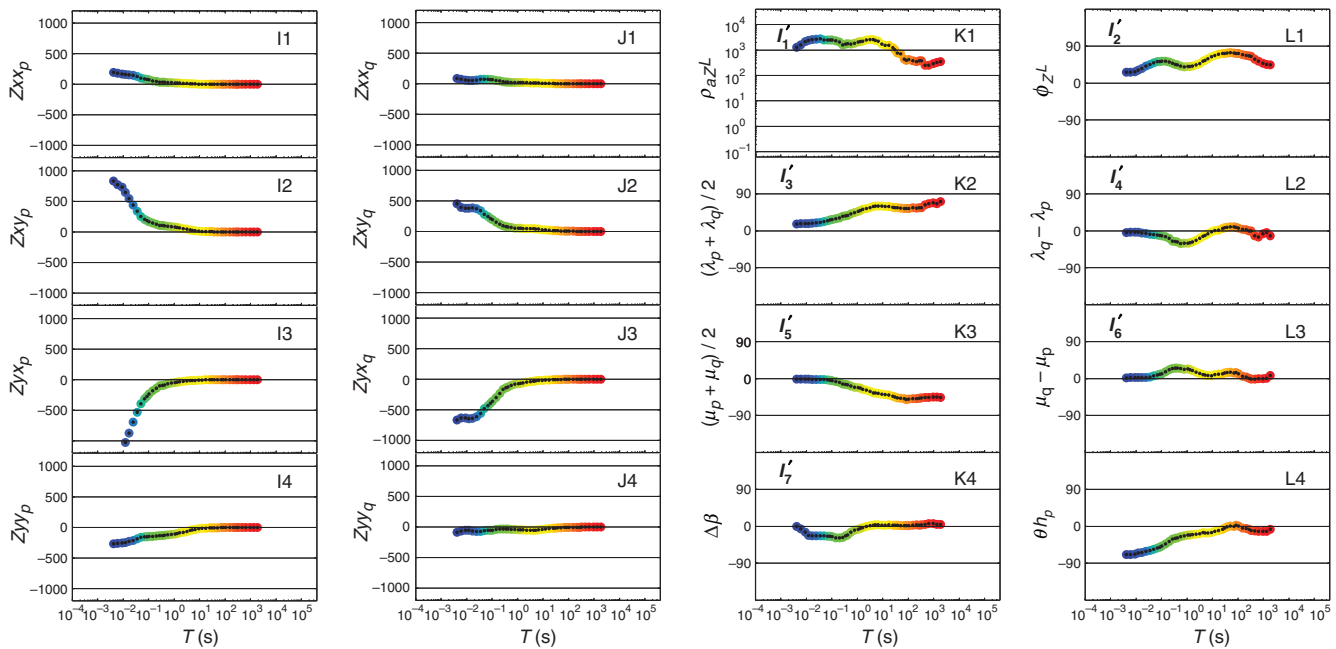
Fig. 9. Summary of the MT data for site NQ101R, showing on the left the basic tensor elements plotted as functions of period, and on the right their representation by the set of invariants, I'_1 to I'_7, proposed as optimum in this paper. Inspection of the tensor-element plots on the left tells little about the character of the MT recording site, whereas from inspection of the columns on the right information is gained regarding the MT dimensionality of the site and its period dependence. Also, from panel L4, some information is gained about geologic strike. Significantly, for the NQ101R data, the I'_7 quantity $\Delta\beta$ in panel K4 can be seen to be near zero for much of its range.

As period lengthens, the data become both more 2D (as I'_3 increases), and more 3D (as I'_5 increases), with I'_4 and I'_6 giving information on the consistency (or otherwise) of these characteristics between the tensor in-phase and quadrature parts.

At the long-period end of the spectrum the data are now strongly 3D, even extremely so, indicated by the values of I'_3 approaching 90° with significant values of I'_5. The in-phase and quadrature parts of the tensor are in fact both approaching singularity, which is also shown by the long-period (red) circles in panels C1 and D1 of Figure 7 approaching their respective origins of axes.

A particular interest lies in the I'_7 values in panel K4, which for the long-period end of the spectrum remain small while the 2D and 3D indicators I'_3 and I'_5 steadily increase in value. The reason for this behaviour is that the increasing three-dimensionality in the data is of a particular type, in which there is a dominant electric field direction common to both parts of the MT tensor.

Conclusions

This paper has focussed on expressing an observed magnetotelluric tensor as a set of seven rotational invariants, together with a single quantity which is rotation dependent. Attention has been given to expressing the invariants diagrammatically, as an aid to understanding their behaviour and significance.

Results for an example observing site (NQ101R) demonstrate that it is straightforward to compute such invariants as a function of period. Particular characteristics of the dimensionality of the data are commonly then shown to be period-dependent.

Attention has focussed in this paper on a newly-recognised invariant $\Delta\beta$ which in the example shown is found, perhaps unexpectedly, to be near zero even when other indications of three-dimensionality are high. In the context of the complications possible in 3D geological structures, low $\Delta\beta$

values indicate a simplifying feature which may prove to be an aid in the interpretation and modelling of MT data.

Conflicts of interest

The author declares no conflicts of interest.

References

Bahr, K., 1988, Interpretation of the magnetotelluric impedance tensor: regional induction and local telluric distortion: *Journal of Geophysics*, **62**, 119–127.

Bahr, K., 1991, Geological noise in magnetotelluric data: a classification of distortion types: *Physics of the Earth and Planetary Interiors*, **66**, 24–38. doi:10.1016/0031-9201(91)90101-M

Berdichevsky, M. N., and Dimitriev, V. I., 1976, Basic principles of interpretation of magnetotelluric curves, *in* A. Adam, ed., *Geoelectric and geothermal studies*, KAPG geophysical monograph: Akademiai Kaido Budapest, 165–221.

Berdichevsky, M. N., and Dmitriev, V. I., 2008, *Models and methods of magnetotellurics*: Springer.

Caldwell, T. G., Bibby, H. M., and Brown, C., 2004, The magnetotelluric phase tensor: *Geophysical Journal International*, **158**, 457–469. doi:10.1111/j.1365-246X.2004.02281.x

Chave, A. D., and Jones, A. G., eds., 2012, *The magnetotelluric method: theory and practice*: Cambridge University Press.

Hobbs, B. A., 1992, Terminology and symbols for use in studies of electromagnetic induction in the Earth: *Surveys in Geophysics*, **13**, 489–515. doi:10.1007/BF01903487

Ingham, M. R., 1988, The use of invariant impedances in magnetotelluric interpretation: *Geophysical Journal of the Royal Astronomical Society*, **92**, 165–169. doi:10.1111/j.1365-246X.1988.tb01130.x

Jones, A. G., 2012, Distortion of magnetotelluric data: its identification and removal, *in* A. D. Chave, and A. G. Jones, eds., *The magnetotelluric method: theory and practice*: Cambridge University Press, 219–302.

Lilley, F. E. M., 1993, Magnetotelluric analysis using Mohr circles: *Geophysics*, **58**, 1498–1506. doi:10.1190/1.1443364

Lilley, F. E. M., 1998, Magnetotelluric tensor decomposition: Part I, Theory for a basic procedure: *Geophysics*, **63**, 1885–1897. doi:10.1190/1.1444481

Lilley, F. E. M., 2012, Magnetotelluric tensor decomposition: insights from linear algebra and Mohr diagrams, *in* H. S. Lim, ed., *New achievements in geoscience*: InTech Open Science, 81–106.

Lilley, F. E. M., 2016, The distortion tensor of magnetotellurics: a tutorial on some properties: *Exploration Geophysics*, **47**, 85–99. doi:10.1071/EG14093

Marti, A., 2014, The role of electrical anisotropy in magnetotelluric responses: from modelling and dimensionality analysis to inversion and interpretation: *Surveys in Geophysics*, **35**, 179–218. doi:10.1007/s10712-013-9233-3

Marti, A., Queralt, P., Jones, A. G., and Ledo, J., 2005, Improving Bahr's invariant parameters using the WAL approach: *Geophysical Journal International*, **163**, 38–41. doi:10.1111/j.1365-246X.2005.02748.x

Marti, A., Queralt, P., and Ledo, J., 2009, WALDIM: a code for the dimensionality analysis of magnetotelluric data using the rotational invariants of the magnetotelluric tensor: *Computers & Geosciences*, **35**, 2295–2303. doi:10.1016/j.cageo.2009.03.004

Marti, A., Queralt, P., Ledo, J., and Farquharson, C., 2010, Dimensionality imprint of electrical anisotropy in magnetotelluric responses: *Physics of the Earth and Planetary Interiors*, **182**, 139–151. doi:10.1016/j.pepi.2010.07.007

Simpson, F., and Bahr, K., 2005, *Practical magnetotellurics*: Cambridge University Press.

Strang, G., 2003, *Introduction to linear algebra* (3rd edition): Wellesley–Cambridge Press.

Szarka, L., and Menvielle, M., 1997, Analysis of rotational invariants of the magnetotelluric impedance tensor: *Geophysical Journal International*, **129**, 133–142. doi:10.1111/j.1365-246X.1997.tb00942.x

Weaver, J. T., Agarwal, A. K., and Lilley, F. E. M., 2000, Characterization of the magnetotelluric tensor in terms of its invariants: *Geophysical Journal International*, **141**, 321–336. doi:10.1046/j.1365-246x.2000.00089.x

Weidelt, P., and Chave, A. D., 2012, The magnetotelluric response function, *in* A. D. Chave, and A. G. Jones, eds., *The magnetotelluric method: theory and practice*: Cambridge University Press, 122–164.

Young, H. D., and Freedman, R. A., 2016, *University physics with modern physics* (14th edition): Pearson Global.

Appendix A

Details of the Bahr analysis shown by a Mohr diagram

The axes rotation angles α_1 and α_2 introduced in the section *The Bahr (1988) analysis* and Figure 5 are shown in more detail in Figure A-1.

In an ideal Bahr case, $(\alpha_1 + \pi - \alpha_2)$ will have the value 90°. It can be seen in Figure A-1, diametrically opposite the point marked with a star, that this condition is close to being satisfied in the present case. In such circumstances, where α_1 and α_2 both exist, the WAL2000 invariant I_7 may be obtained from the departure of $(\alpha_1 + \pi - \alpha_2)$ from 90°. Call this departure angle ϵ. Then

$$\epsilon = 90° - (\alpha_1 + 180° - \alpha_2) \tag{A-1}$$

$$= \alpha_2 - \alpha_1 - 90° \tag{A-2}$$

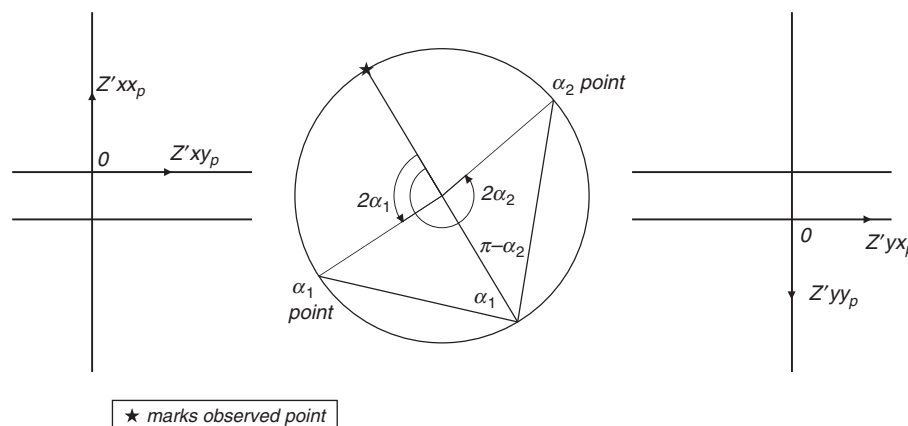and the sine of the amplitude of ϵ is taken as I_7.

Fig. A-1. This figure repeats part of Figure 5, with some details omitted so that other details, now added, are clearer to see. At the point on the circle diametrically opposite the star, the Bahr rotation angles α_1 and α_2 are shown as α_1 and $(\pi - \alpha_2)$. It can be seen that $(\alpha_1 + \pi - \alpha_2)$ is close to 90°; thus α_2 is close to $(\alpha_1 + 90°)$, and $(\alpha_2 - \alpha_1)$ is close to 90°. The I_7 of Equation 66 is the sine of the difference between $(\alpha_2 - \alpha_1)$ and 90° and is thus, in this instance, the sine of a small angle (3.8°).

Appendix B

Clarification of computations of the I_7 of WAL2000

Using their notation, equations 48 and 49 of Weaver et al. (2000) are

$$Q\sin(2\theta_1 - 2\theta') - d_{41} + d_{23} = 0 \tag{B-1}$$

and

$$Q\sin(2\theta' - 2\theta_2) - d_{41} + d_{23} = 0 \tag{B-2}$$

where θ_1 and θ_2 are strike directions, θ' is a 'mean strike direction', and d_{41} and d_{23} are calculated from values of an observed MT tensor. Using the relationship

$$I_7 = (d_{41} - d_{23})/Q \tag{B-3}$$

Equations B-1 and B-2 become, respectively,

$$\sin(2\theta_1 - 2\theta') = I_7 \tag{B-4}$$

and

$$\sin(2\theta' - 2\theta_2) = I_7 \tag{B-5}$$

In turn these equations give

$$\theta_1 = \frac{1}{2}\arcsin(I_7) + \theta' \tag{B-6}$$

and

$$\theta_2 = \theta' - \frac{1}{2}\arcsin(I_7) \tag{B-7}$$

Subtracting Equation B-7 from Equation B-6 gives

$$\theta_1 - \theta_2 = \arcsin(I_7) \tag{B-8}$$

and so

$$\sin(\theta_1 - \theta_2) = I_7 \tag{B-9}$$

as in Weaver et al. (2000) with the implication that when $I_7 = 0$, the equalities $\theta_1 = \theta_2 = \theta'$ accompany galvanic distortion in a 2D region.

However note that for $I_7 = 0$ Equation B-4 has the solution

$$2\theta_1 - 2\theta' = 0, \pm\pi \tag{B-10}$$

and Equation B-5 has the solution

$$2\theta' - 2\theta_2 = 0, \pm\pi \tag{B-11}$$

leading upon the addition of Equations B-10 and B-11 to

$$\theta_1 - \theta_2 = 0, \pm\pi/2, \pm\pi \tag{B-12}$$

Then, rather than take $\theta_1 = \theta_2$ as in Weaver et al. (2000) it is clearer, as shown in Figure 5, to think of $\theta_2 = \theta_1 + \pi/2$ for galvanic distortion in a 2D region. That is, θ_2 should not be thought of as departing from θ_1 (and so equal to θ_1 in an ideal situation), but as departing from $\theta_1 + \pi/2$ (and so equal to $\theta_1 + \pi/2$ in an ideal situation). By way of illustration, in Figure A-1 the angles α_1 and α_2 are not approximately the same, but are different by close to 90°.